THE JOURNAL OF BIOLOGICAL CHEMISTRY VOL. 286, NO. 34, pp. 30022–30033, August 26, 2011

Encephalopathy Caused by Ablation of Very Long Acyl Chain Ceramide Synthesis May Be Largely Due to Reduced Galactosylceramide Levels*[S]

Received for publication, May 16, 2011, and in revised form, June 22, 2011 Published, JBC Papers in Press, June 24, 2011, DOI 10.1074/jbc.M111.261206

Oshrit Ben-David[‡], Yael Pewzner-Jung[‡], Ori Brenner[§], Elad L. Laviad[‡], Aviram Kogot-Levin[¶], Itai Weissberg[‖], Inbal E. Biton[§], Reut Pienik[‡], Elaine Wang[**], Samuel Kelly[**], Joseph Alroy[‡‡], Annick Raas-Rothschild[¶], Alon Friedman[‖], Britta Brügger[§§], Alfred H. Merrill, Jr.[**], and Anthony H. Futerman[‡1]

From the Departments of [‡]Biological Chemistry and [§]Veterinary Resources, Weizmann Institute of Science, Rehovot 76100, Israel, [¶]Department of Human Genetics and Metabolic Diseases, Hadassah Hebrew University Medical Center, Jerusalem 91120, Israel, [‖]Department of Physiology and Neurobiology, Zlotowski Center for Neuroscience, Ben-Gurion University of the Negev, Beer-Sheva 84105, Israel, [**]School of Biology and Petit Institute for Bioengineering and Bioscience, Georgia Institute of Technology, Atlanta, Georgia 30332-0230, [‡‡]Department of Pathology, Tufts University Schools of Medicine and Veterinary Medicine and Tufts Medical Center, Boston, Massachusetts 01536, and [§§]Heidelberg University Biochemistry Center, Im Neuenheimer Feld 328, 69120 Heidelberg, Germany

Sphingolipids (SLs) act as signaling molecules and as structural components in both neuronal cells and myelin. We now characterize the biochemical, histological, and behavioral abnormalities in the brain of a mouse lacking very long acyl (C22–C24) chain SLs. This mouse, which is defective in the ability to synthesize C22–C24-SLs due to ablation of ceramide synthase 2, has reduced levels of galactosylceramide (GalCer), a major component of myelin, and in particular reduced levels of non-hydroxy-C22–C24-GalCer and 2-hydroxy-C22–C24-GalCer. Noteworthy brain lesions develop with a time course consistent with a vital role for C22–C24-GalCer in myelin stability. Myelin degeneration and detachment was observed as was abnormal motor behavior originating from a subcortical region. Additional abnormalities included bilateral and symmetrical vacuolization and gliosis in specific brain areas, which corresponded to some extent to the pattern of ceramide synthase 2 expression, with astrogliosis considerably more pronounced than microglial activation. Unexpectedly, unidentified storage materials were detected in lysosomes of astrocytes, reminiscent of the accumulation that occurs in lysosomal storage disorders. Together, our data demonstrate a key role in the brain for SLs containing very long acyl chains and in particular GalCer with a reduction in their levels leading to distinctive morphological abnormalities in defined brain regions.

Ceramide, the lipid backbone of all complex sphingolipids (SLs),[2] is an important signaling molecule and an intermediate in the pathway of SL biosynthesis. Ceramide plays a key role in brain development (1–3), and modulating its levels or modulating the signaling pathways in which it is involved (4–6) affects neuronal development. In mammals, ceramide is synthesized *de novo* by *N*-acylation of a sphingoid long chain base, which is catalyzed by a family of six enzymes, the ceramide synthases (CerS), each of which uses a restricted subset of acyl-CoAs for *N*-acylation. Thus, CerS1 uses C18-CoA (7), CerS4 uses C18- and C20-CoAs (8), CerS5 and CerS6 use C16-CoA (8, 9), and CerS3 uses C26-CoA and higher (Ref. 10; for a review, see Ref. 11). CerS2 utilizes very long acyl chain CoAs (*i.e.* C22–C24) and is expressed at the highest levels and displays the widest tissue distribution of all CerS (12). The expression pattern of the CerS and their structural features, localization, and regulation have been reviewed (13).

We recently generated a CerS2-null mouse (14). This mouse displayed increased rates of hepatocyte apoptosis and proliferation and severe, progressive hepatopathy (15), which was due to either a decrease in very long acyl chain SLs (C22–C24) or an increase in C16-ceramide or sphinganine, both of which were unexpectedly elevated in the liver (14). We have now examined brain abnormalities in the CerS2-null mouse. Although CerS2 mRNA expression levels are significantly lower in the whole brain than in the liver (12), it might be expressed at higher levels in a subset of brain cells, such as oligodendrocytes (16), and SLs containing very long acyl chain fatty acids are abundant in white matter and in myelin (17, 18), suggesting a key role for CerS2 in these cells and brain regions. A previous report demonstrated that CerS2-null mice exhibit myelin defects as well as cerebellar degeneration at 9 months of age and cell loss in the hippocampus (19). However, no changes in other brain regions were described, and no systematic evaluation of the lesions was performed such that the relationship between very long acyl chain SLs and brain dysfunction could not be ascertained.

We now show that CerS2-null mice exhibit profound alterations in lipid composition in both whole brain and

* This work was supported, in whole or in part, by National Institutes of Health Grant GM076217. This work was also supported by Israel Science Foundation Grant 1404/07, the Minerva Foundation, and Merck KGaA.

[S] The on-line version of this article (available at http://www.jbc.org) contains supplemental Movie 1, Fig. 1, and Tables 1 and 2.

[1] The Joseph Meyerhoff Professor of Biochemistry at the Weizmann Institute of Science. To whom correspondence should be addressed. Tel.: 972-8-9342704; Fax: 972-8-9344112; E-mail: tony.futerman@weizmann.ac.il.

[2] The abbreviations used are: SL, sphingolipid; CerS, ceramide synthase(s); CGT, ceramide-UDP galactosyltransferase; FA2H, fatty acid 2-hydroxylase; GalCer, galactosylceramide; GlcCer, glucosylceramide; HexCer, hexosylceramide; MBP, myelin basic protein; PLP, proteolipid protein; SM, sphingomyelin; NBD, 4-nitrobenzo-2-oxa-1,3-diazole; GP, globus pallidus; GFAP, glial fibrillary acidic protein.

purified myelin and in particular reduced levels of non-hydroxy-C22–C24-GalCer and 2-hydroxy-C22–C24-GalCer. These changes are accompanied by pronounced bilateral and symmetrical astrogliosis and by mild bilateral and symmetrical vacuolization in various white and gray matter regions along with microglial activation in defined brain areas. In addition, CerS2-null mice exhibit neurological abnormalities originating from a subcortical region and accumulation of unidentified storage materials in lysosomes of astrocytes.

EXPERIMENTAL PROCEDURES

Materials—D-*erythro*-[4,5-^{3}H]Sphinganine was synthesized as described (20). Fatty acyl-CoAs, C6-NBD-sphingomyelin (SM), C6-NBD-GalCer, and the internal standards for liquid chromatography electrospray ionization tandem mass spectrometry (LC-ESI MS/MS) were from Avanti (Alabaster, AL). A ganglioside standard was from Matreya (Pleasant Gap, PA). The following antibodies were used: mouse anti-glyceraldehyde-3-phosphate dehydrogenase (Millipore, Darmstadt, Germany), rat anti-myelin basic protein (MBP) (Abcam, Cambridge, MA), mouse anti-proteolipid protein (PLP) (Sigma-Aldrich); rabbit anti-glial fibrillary acidic protein (GFAP) (AbD Serotec, Oxford, UK), rat anti-Mac2 (Cedarlane, Ontario, Canada), and mouse anti-neuronal nucleus antibody (Chemicon, Temecula, CA).

Mice—Mice were generated as reported (14), maintained under specific pathogen-free conditions, and handled according to protocols approved by the Weizmann Institute Animal Care Committee according to international guidelines.

Lipid Analysis—SL analysis by LC-ESI MS/MS was performed using a PE-Sciex API 3000 triple quadrupole mass spectrometer and an ABI 4000 quadrupole-linear ion trap mass spectrometer (12, 14, 21). For 2-hydroxyhexosylceramide (2-hydroxy-HexCer), the same method was used as for determining glucosylceramide and galactosylceramide but with addition of the precursor-product ion pairs for 2-hydroxy-HexCer. Total glycerolipid (pmol/mg dry weight) and cholesterol levels were measured by nano-ESI MS/MS (22, 23) and expressed as a percentage of total glycerolipid levels.

Enzyme Activities—Enzyme activities were determined as follows: CerS2 using D-*erythro*-[4,5-^{3}H]sphinganine and C24-acyl-CoA (12, 24); neutral and acid sphingomyelinase using C6-NBD-SM (14, 25, 26); galactosylceramidase using C6-NBD-GalCer (27); and hexosaminidase A, α-galactosidase, β-glucuronidase, α-mannosidase, β-mannosidase, and *p*-nitrocatechol sulfate using 4-methylumbelliferone (28–30). Gangliosides were purified (31) after isolation from the upper phase (32), separated by thin layer chromatography using chloroform, methanol, 0.2% $CaCl_2$ (55:45:10) as the developing solvent, and stained using resorcinol (33). Gangliosides were identified using authentic ganglioside standards.

Myelin Purification—Brain tissue was homogenized in 0.25 M sucrose, 10 mM Hepes, pH 7.4, 2 mM EGTA. The supernatant was collected after centrifugation (3 min at 800 $\times$ g_{av} at 4 °C) and placed on top of a sucrose gradient comprising 2, 1.4, 0.85, and 0.25 M sucrose. After centrifugation (20 h at 70,000 $\times$ g_{av} at 4 °C), the crude myelin fraction was collected from the gradient, and its identity was confirmed by Western blotting using an anti-MBP antibody. The crude myelin fractions underwent four consecutive osmotic shocks followed by centrifugation (15 min at 75,000 $\times$ g_{av} at 4 °C one time and then three times for 10 min at 12,000 $\times$ g_{av} at 4°) (34) and then resuspension in water.

Immunohistochemistry—Tissues were collected at necropsy and fixed by immersion in 10% neutral buffered formalin. Tissues were processed routinely, embedded in paraffin, trimmed at 4–5 μm, and stained with hematoxylin and eosin or with toluidine blue. Immunohistochemistry was performed on paraformaldehyde-perfused tissues using an immunoperoxidase procedure with diaminobenzidine as the chromogen (35). Rabbit anti-GFAP (1:4,000 dilution) and rat anti-Mac2 (1:1,000 dilution) antibodies were used to detect astrocytes and microglia, respectively.

For X-Gal (5-bromo-4-chloro-3-indolyl-β-galactoside) staining, tissues were frozen at −20 °C and embedded in optimal cutting temperature (OCT) Tissue-Tek. 20-μm sections were fixed with 0.2% glutaraldehyde in phosphate-buffered saline, rinsed three times in wash buffer (100 mM phosphate-buffered saline, pH 7.4, 2 mM $MgCl_2$, 5 mM EGTA, 0.01% sodium deoxycholate, 0.02% Nonidet-P40), and stained with β-galactosidase substrate buffer (as above but supplemented with 5 mM $K_3[Fe(CN)_6]$, 5 mM $K_4[Fe(CN)_6]$, and 1 mg/ml X-Gal) overnight at 37 °C in the dark.

Electron Microscopy—Mice were perfused with 3% paraformaldehyde, 2% glutaraldehyde in cacodylate buffer containing 5 mM $CaCl_2$, pH 7.4. Brains were removed, fixed for 30 min prior to cutting with a Vibratome into 200-μm slices, and fixed again for 2 h at room temperature and for 12 h at 4 °C. After washing, tissue slices were postfixed in osmium tetroxide, 0.5% potassium dichromate, 0.5% potassium hexacyanoferrate in cacodylate buffer for 1 h and embedded in EMbed 812 (Electron Microscopy Sciences, Hatfield, PA). Epon blocks were cut into small pieces, re-embedded followed by preparation of 70–100-nm ultrathin slices, and mounted onto grids for analysis in a Philips CM-12 FEI electron microscope. Images were captured with an Eagle 2kx2k FEI camera (FEI, Eindhoven, Netherlands).

Western Blotting—Western blotting was performed (15) using the following antibodies, which were diluted in phosphate buffer with 0.1% Tween 20: rat anti-MBP (1:1,000 dilution), mouse anti-PLP (1:1,000 dilution), and mouse anti-glyceraldehyde-3-phosphate dehydrogenase (1:5,000 dilution). Densitometry was performed using ImageQuant software (Amersham Biosciences), and expression levels were normalized to glyceraldehyde-3-phosphate dehydrogenase levels.

Neuronal Counting—Brain sections were stained with an anti-neuronal nucleus antibody (1:250). Twenty images were captured at different magnifications, and cells were counted using ImageJ.

Telemetric Electroencephalogram (EEG) and Video Monitoring—Mice were implanted with a telemetric system for EEG monitoring (Data Science International; Ref. 36). A transmitter (TA10EA-F20) was placed subcutaneously on the right dorsal side of a stereotactically fixed, deeply anesthetized animal (0.8–1.2% isoflurane). In each hemisphere, a hole was drilled through the skull using a surgical drill, and stainless steel screws serving as electrodes were inserted through the drilled holes to the epi-

dural space. The epicranial side of each screw was connected to a transmitter lead and secured with bone cement. Mice were allowed 1 week to recover from the acute affects of surgery. Starting from day 7, the freely moving mice were monitored for 1 week. EEG was recorded at 1 KHz and analyzed off line using Matlab® scripts. Power spectral density was calculated (37) and normalized to maximum power for each mouse. 7,200 1-s windows with 0.5-s overlap were randomly selected and analyzed from six different time periods for each mouse ($n = 5$).

Magnetic Resonance Imaging—Magnetic resonance imaging (MRI) was performed on a 9.4-tesla BioSpec Magnet 94/20 USR system (Bruker). The MRI protocol included a transverse relaxation time (T_2) map, which was acquired using the multislice spin echo imaging sequence with the following parameters: time of repetition of 3000 ms, 16 time echo increments (linearly from 10 to 160 ms), matrix dimension of 256 × 128, and two averages. Twenty continuous slices with a slice thickness of 1 mm were acquired with a field of view of 22 × 22 mm^2.

In vivo brain MRI (five control mice and five CerS2-null mice) was performed. During the MRI scanning, mice were anesthetized with isoflurane (5% for induction and 1–2% for maintenance) mixed with O_2 (1 liter/min) delivered through a nasal mask. A quantitative T_2 map was produced from multiecho T_2-weighted images. The multiecho signal was fitted to a monoexponential decay to extract the T_2 value for each image pixel. Processing and analysis of the MRI data were performed using different in-house programs in Matlab, producing an averaged value for the entire brain.

Statistics—Statistical significance was assessed using an unpaired, one-tailed, Student's t test with a p value of <0.05 considered statistically significant.

RESULTS

SL Acyl Chain Composition in CerS2-null Mouse Brain— CerS2 activity is much lower in brain homogenates (50 ± 9 pmol/min/mg) than in liver (~200–300 pmol/min/mg) (12) and is virtually absent in the brain of CerS2-null mice (2 ± 2.5 pmol/min/mg, $n = 5$). As a consequence, the CerS2-null mouse has very low levels of C22–C24-ceramide and C22–C24-SM (14) with a proportional increase in C18-ceramide and C18-SM (Fig. 1). In newborn (P0) wild type (WT) mice, most of the ceramide and SM contains C18-acyl chains (presumably synthesized by CerS1 (7, 16)) with lower levels of C22–C24; this distribution does not change significantly up to 4 months of age (Fig. 1). Substantial levels of C16-ceramide and C16-SM are found immediately after birth and decrease during development in both CerS2-null and WT mice, consistent with the decreased expression of CerS6 during brain development (38). In contrast, the acyl chain composition of HexCer (which consists of both glucosylceramide (GlcCer) and galactosylceramide (GalCer)) changes dramatically during development. WT mice have mainly C18-HexCer at birth, but C22–C24-HexCer becomes the dominant species by 1 month of age (39), and by 4 months, C18-HexCer comprises <10% of the total HexCer (Fig. 1 and supplemental Table 1). This suggests that any pathological changes resulting from the altered HexCer acyl chain composition (Fig. 1) might begin between P0 and 1 month, a period of active myelination (40).

Acyl Chain Composition of Non-hydroxy-GalCer and 2-Hydroxy-GalCer—The elevation in C18-ceramide and in C18-SM in the CerS2-null mice compensates for the loss of C22–C24-ceramide and C22–C24-SM, respectively, such that total levels of ceramide and SM are essentially unaltered (Fig. 1) (19). In contrast, HexCer levels were reduced by ~85% in CerS2-null mice (Fig. 1 and supplemental Table 1). Most brain HexCer consists of GalCer with a ratio of GalCer to GlcCer of ~100:1 in adult mice (Refs. 39 and 41 and Fig. 2). GalCer consists of two major species, 2-hydroxy-GalCer (OH-GalCer) (42) and non-hydroxy-GalCer (non-OH-GalCer), with the former comprising ~50% of the total GalCer (43). No LC-ESI MS/MS standards are currently available for OH-GalCer, precluding rigorous quantification of its amounts, but because Gal-based HexCer comprises the vast majority of HexCer in adult brain (see above), we assume that most of the OH-HexCer measured in the LC-ESI MS/MS analyses consists of OH-GalCer (referred to hereafter as OH-Gal(Hex)Cer). Levels of OH-Gal(Hex)Cer were only reduced by ~40% (Fig. 2*B*). The difference in the reduction of OH-Gal(Hex)Cer levels compared with non-OH-GalCer can be explained by elevation of C18-OH-Gal(Hex)Cer (Fig. 2, *A* and *B*), which compensates to some extent for the loss of C22–C24-OH-Gal(Hex)Cer, whereas there was a much lower elevation of C18-non-OH-GalCer (Fig. 2, *A* and *B*). No changes in total GlcCer levels were apparent (Fig. 2*C*) due to compensation by elevated levels of C18/C18:1-GlcCer (Fig. 2*C*); also in contrast to the ceramide-UDP galactosyltransferase (CGT)−/− mouse, GlcCer levels were not elevated upon reduction in GalCer (41, 44). Thus, the major changes in the SL composition of the CerS2-null mouse brain are (i) a loss in C22–C24-non-OH-GalCer, (ii) a loss in C22–C24-OH-Gal(Hex)Cer, and (iii) an increase in C18-OH-Gal(Hex)Cer.

Previous studies have shown that overexpression of CerS1, which synthesizes C18-ceramide, can alter levels of downstream glycosphingolipids such as neutral glycosphingolipids and gangliosides (7). However, despite changes in the acyl chain composition of glycosphingolipids, the CerS2-null mouse displayed similar levels of gangliosides GD1a, GD1b, and GT1b and a small but inconsistent reduction in GM1 levels (supplemental Fig. 1) (67). Moreover, there were no major changes in levels of sphingoid long chain bases (Fig. 2*D*) with a 2–3-fold elevation of sphinganine levels. This is in contrast to the CerS2-null mouse liver where sphinganine levels are elevated by 50–100-fold (14), implying that changes in long chain base levels are unlikely to be responsible for the brain abnormalities. Also in contrast to liver (14), no changes were observed in neutral sphingomyelinase activity (6.3 ± 1.5 μmol/mg/min in WT mouse brain and 6.4 ± 1.3 μmol/mg/min in CerS2-null mouse brain).

Myelin SL and Acyl Chain Composition—Because major changes in GalCer acyl chain composition occur during the 1st month of life (Fig. 1) and because GalCer is a major lipid component of oligodendrocytes and myelin (45), we analyzed SL levels and acyl chain composition in purified myelin by LC-ESI MS/MS. A similar pattern was observed as in whole brain with no change in ceramide, SM, GlcCer, and lactosylceramide and a reduction in GalCer (Fig. 3*A* and supplemental Table 2). Elevated levels of C18-ceramide and C18-SM accounted for the

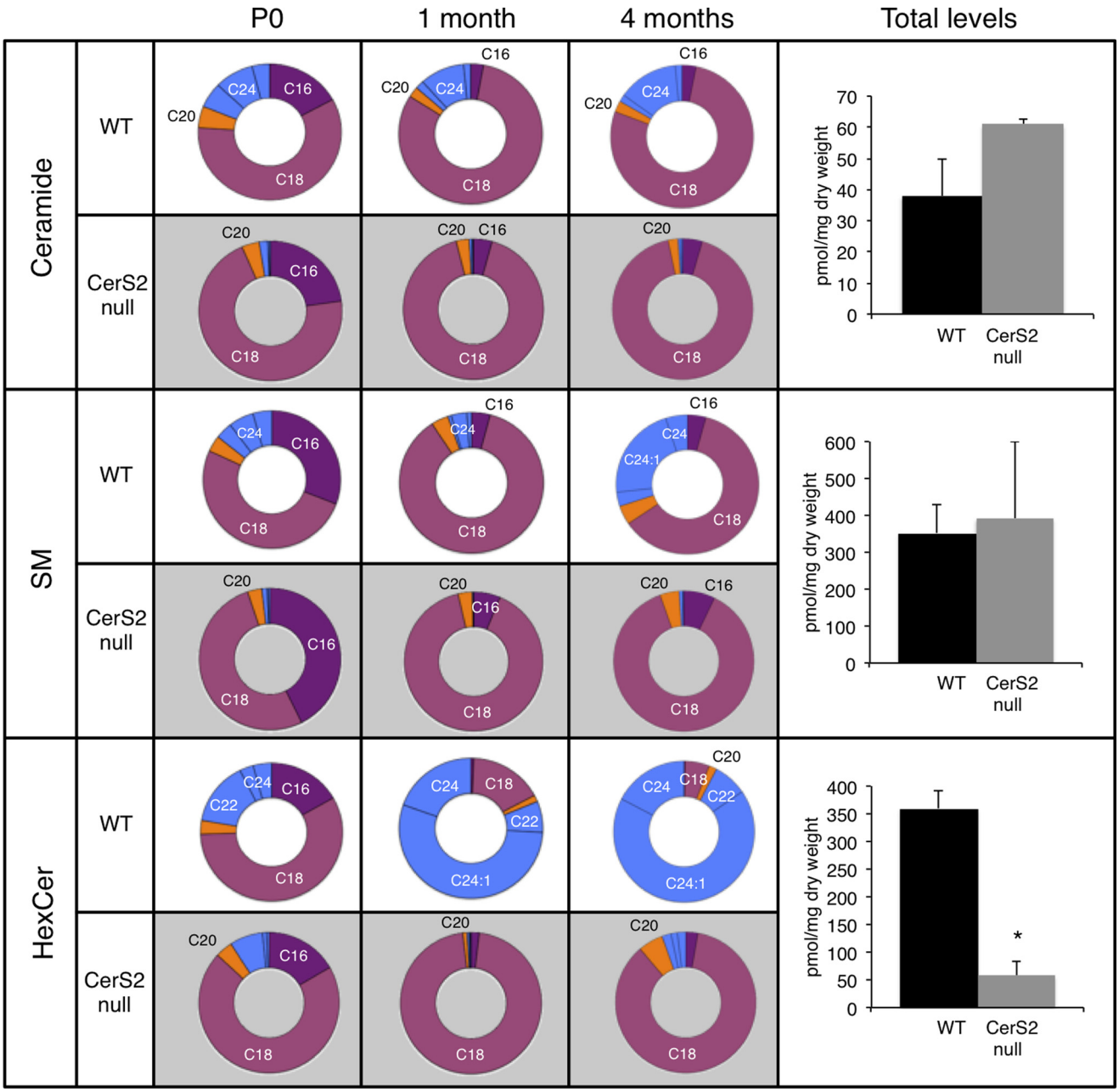

FIGURE 1. **LC-ESI MS/MS analysis of acyl chain distribution and total SL levels in CerS2-null mouse brain.** The pie charts show the acyl chain distribution at P0, 1 month, and 4 months of age as a percentage of the total. The *right-hand column* shows total SL levels in 4-month-old brains. Supplemental Table 1 gives HexCer levels in pmol/mg of tissue. Data are from two mice for which triplicate analyses were performed ± S.D., *, $p < 0.01$.

lack of change of total ceramide and SM levels (Fig. 3*B*). Although some C22–C24-GlcCer and C22–C24-GalCer were detectable in myelin (Fig. 3*B* and supplemental Table 2), their levels were extremely low (Fig. 3*A*). Thus, changes in brain SL levels and in their acyl chain composition appear to largely reflect changes in myelin.

Finally, we analyzed cholesterol and glycerolipid levels. No changes were detected in sterol levels with the exception of a small increase in cholesterol esters. However, because levels of cholesterol esters are extremely low in brain (~1 pmol/mg dry weight compared with 130 pmol/mg dry weight for cholesterol), this change is unlikely to be of any pathological consequence. Likewise, no changes were observed in glycerolipid levels (phosphatidylcholine, 44% of total glycerolipids in WT and 41% in CerS2-null; phosphatidylethanolamine, 35 *versus* 39%; phosphatidylserine, 18 *versus* 15%; phosphatidylinositol, 3 *versus* 4%; and phosphatidylglycerol, 0.3% for both WT and CerS2-null).

Vacuolization in Gray and White Matter Regions—Abnormalities were detected in the CerS2-null mouse brain by ~4 months of age (Fig. 4), characterized by a subtle encephalopathy with minimal to moderate bilateral and symmetrical vacuolization and gliosis. Round to oval vacuoles (4–30 μm in diameter) were observed in multiple regions of the brain in both gray and white matter regions but predominated in the former. Such vacuoles are never found in WT brains. In the cerebral cortex,

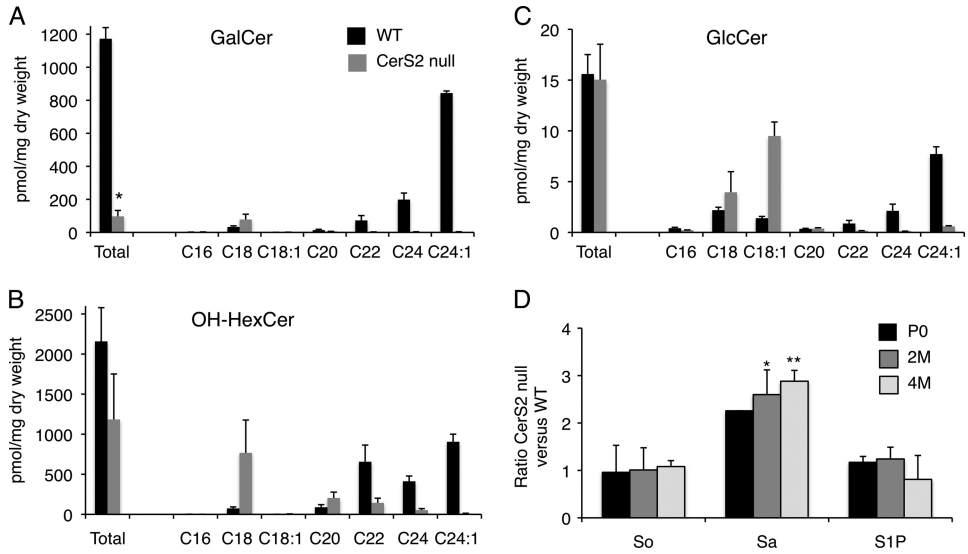

FIGURE 2. **Total HexCer and long chain base levels in 4-month-old mice.** Total GalCer (*A*), OH-HexCer (*B*), and GlcCer (*C*) levels and acyl chain distribution are shown. The *left-hand columns* show total HexCer levels, and the other columns show levels of individual acyl chains. Values are means ± S.D. for which duplicate analyses were performed ($n = 2$). *, $p < 0.01$. *D*, -fold change in CerS2-null *versus* WT mice for the long chain bases sphingosine (*So*), sphinganine (*Sa*), and sphingosine 1-phosphate (*S1P*) at different ages: newborn (*P0*), 2 months (*2M*) of age, and 4 months (*4M*) of age. Values are means ± S.D. ($n = 2$). *, $p < 0.05$; **, $p < 0.01$.

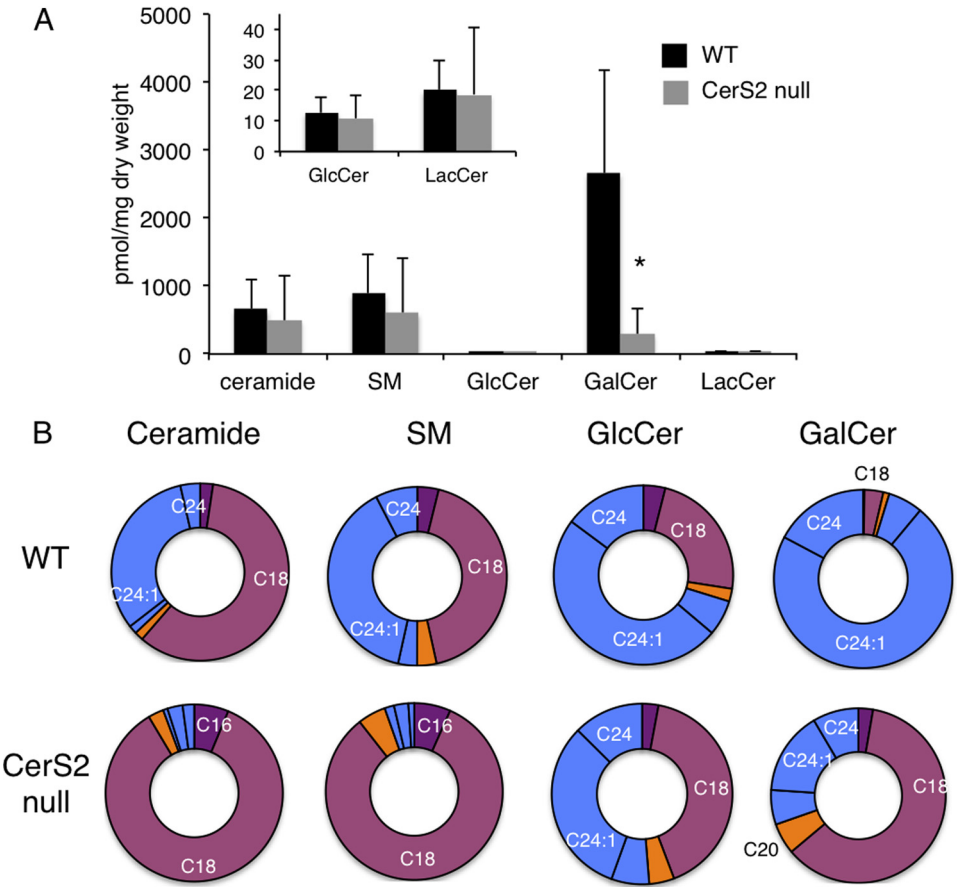

FIGURE 3. **LC-ESI MS/MS analysis of SL composition of myelin.** *A*, total SL levels in purified myelin. The *inset* shows levels of GlcCer and lactosylceramide (*LacCer*). *, $p < 0.05$. *B*, acyl chain distribution of myelin. Supplemental Table 2 gives SL levels in pmol/mg of tissue. Values are means ± S.D. ($n = 3$) in which two analyses were performed on 3-month-old mice and one analysis was performed on 5-month old mice with no significant differences between them.

vacuoles were most common in the frontal and parietal lobes in the motor cortex, the cingulate gyrus, and the retrosplenial cortex; this is in contrast to a previous study (19), which suggested that vacuolization does not occur in the telencephalon. The septal nuclei were commonly involved. In the thalamus, which was consistently affected (Fig. 4, *A* and *B*), vacuoles tended to be more common in lateral regions but were also present dorsally and ventromedially. In many CerS2-null mice, the most

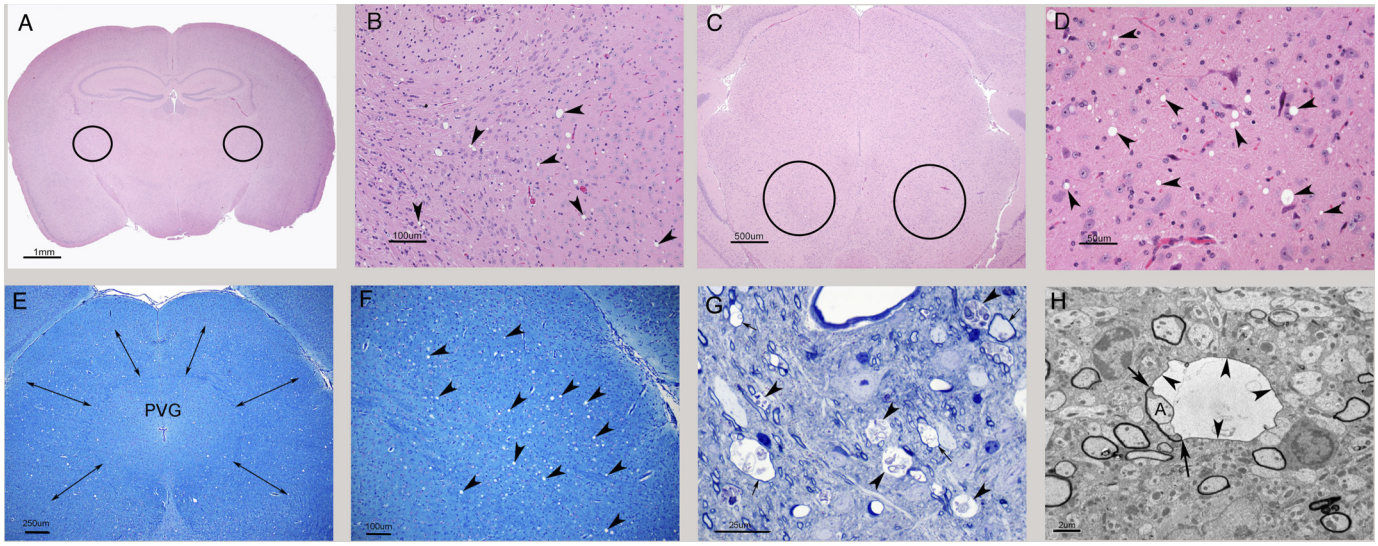

FIGURE 4. **Histological abnormalities.** *A–D*, hematoxylin- and eosin-stained sections. *A*, a coronal section at the level of the thalamus. The *circles* indicate the bilateral and symmetrical location of foci of vacuolization (which cannot be seen at this magnification). *Scale bar*, 1 mm. *B*, higher magnification of a field in *A* showing vacuolization in the lateral thalamus. Vacuoles are indicated by *arrowheads*. Such vacuoles are never found in appropriately prepared WT brains. *Scale bar*, 100 μm. *C*, coronal section of the midbrain at the level of the rostral colliculi. *Circles* indicate bilateral and symmetrical vacuoles. *Scale bar*, 500 μm. *D*, the same foci of vacuolization as in *C*. Vacuoles are indicated by *arrowheads* and are more prevalent than in *B*. *Scale bar*, 50 μm. *E*, Luxol fast blue cresyl echt violet staining of a coronal section at the level of the midbrain from a mouse with moderate encephalopathy. Vacuoles are scattered within the tissue surrounding the periventricular gray matter (*PVG*) spanned by *double-headed arrows*. *Scale bar*, 250 μm. *F*, higher magnification of the *top right-hand corner* of *E*. Vacuoles are marked with *arrowheads*. *Scale bar*, 100 μm. *G*, semithin section of the midbrain stained by toluene blue. Many vacuoles in this image contain debris (*arrowheads*), and some have a thin dark rim consistent with a ballooned myelin sheath (*arrows*). *Scale bar*, 25 μm. *H*, low magnification electron micrograph of the midbrain (from the same sample as *G*). A vacuole delimited by a thin dark rim of myelin (*arrowheads*) can be seen in the *center*. The *arrows* indicate the point at which the ballooned myelin becomes continuous with the intact myelin sheath surrounding an axon (*A*). Note that the surrounding tissue is well preserved and contains several myelinated axons with intact myelin sheaths. *Scale bar*, 2 μm.

severely affected brain region was the midbrain where vacuoles were widely scattered, affecting many areas, including the anterior and posterior colliculi (Fig. 4, *C–F*). More distally in the pons and medulla oblongata, vacuoles were widely distributed but present in lower amounts. Occasionally, vacuolization was noted in the globus pallidus (GP), caudate putamen, hippocampus, occipital lobe, and cerebellum. Affected white matter tracts included the corpus callosum, fimbria, internal capsule, anterior commissure, and precommissural fornix. The severity of vacuolization varied between individual mice and was not age-dependent. A small number of vacuoles contained flocculent debris, and some of these had a thin dark rim suggestive of myelin (Figs. 4, *G* and *H*, and 7*A*).

Astrogliosis and Microglial Activation—Considerable astrogliosis and microglial activation was detected at ~3 months of age with astrogliosis more pronounced than microgliosis. Astrogliosis and microgliosis showed a bilateral and symmetrical distribution and were present in white and gray matter (Table 1). White matter regions with high astrogliosis and microglia activation included the fimbria, parts of the corpus callosum, the internal capsule, and the white matter of the cerebellum (Figs. 5 and 6*A* and Table 1). Moreover, a number of gray matter regions and deep nuclei also showed gliosis, including the basal ganglia, specifically the GP. The GP (together with the caudate putamen) is involved in motor control as are specific nuclei in the thalamus, various areas of the cortex, and several nuclei in the brain stem, all of which displayed glial activation (Figs. 5 and 6*A* and Table 1). Gliosis was also observed in the midbrain (substantia nigra), whereas the hippocampus was less affected (Figs. 5 and 6*A* and Table 1). Despite the high level of activated astroglia and microglia in the GP, no neuronal loss was detected in this region (Fig. 6*B*).

TABLE 1
Astrogliosis in brain regions of the CerS2-null mouse

Brain area	Intensity of GFAP labeling[a]
Cortex	
Motor	++
Sensory	++
Piriform	++
Auditory	+
Occipital	−
Basal ganglia	
Caudate putamen	++
Nucleus accumbens	+
Globus pallidus	+++
Substantia nigra	++
Hippocampus	
CA1	−
CA2/CA3	−
Hippocampal fissure	++
Dentate gyrus	−
White matter tracts	
Anterior commissure	++
Corpus callosum	+++
Fimbria	+++
Internal capsule	+++
Cerebellum (white matter)	+++
Other regions	
Thalamus	++
Midbrain	++
Amygdala	++
Olfactory bulb	−

[a] The number of plus signs indicates the extent of GFAP immunoreactivity in the CerS2-null mouse compared with the WT with "−" indicating no change, "+" indicating a few more GFAP-positive cells, and "+++" indicating extensive numbers of GFAP-positive cells.

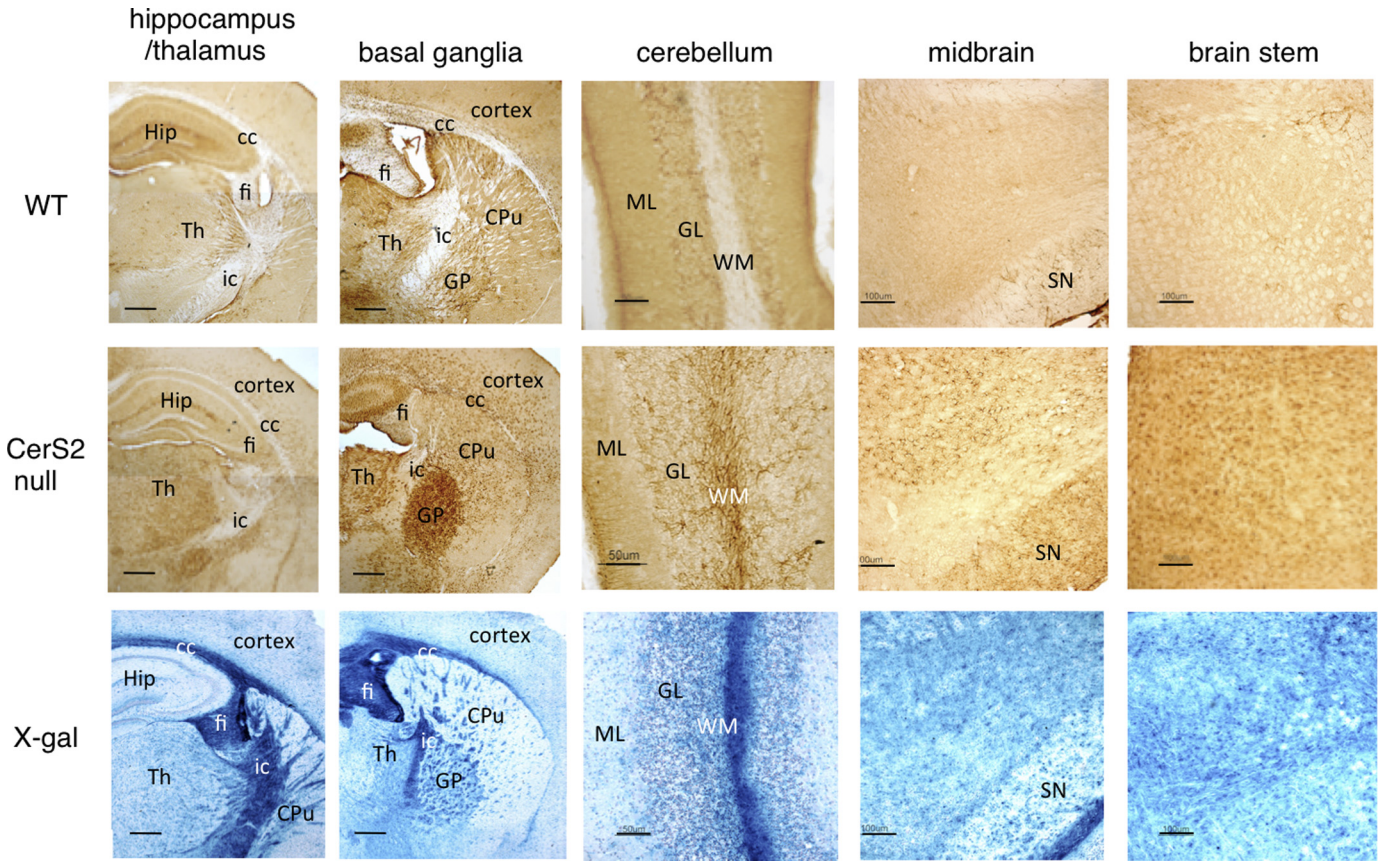

FIGURE 5. **Astrogliosis in various brain regions.** Immunostaining with an anti-GFAP antibody in 4-month-old WT and CerS2-null mice (similar results were obtained at 7 and 10 months) and X-Gal staining from a CerS2-null mouse brain are shown. *CC*, corpus callosum; *CPu*, caudate putamen; *fi*, fimbria; *GL*, granular layer of the cerebellum; *Hip*, hippocampus; *ic*, internal capsule; *ML*, molecular layer of the cerebellum; *SN*, substantia nigra; *Th*, thalamus; *WM*, white matter of the cerebellum. *Scale bars*, 500 μm for basal ganglia and hippocampus, 50 μm for cerebellum, and 100 μm for midbrain and brain stem.

The CerS2-null mouse was generated from a gene trap ES cell clone with LacZ placed under the control of the CerS2 promoter (15). Therefore, β-galactosidase activity (assessed by X-Gal staining) can be used to determine CerS2 promoter activity and expression in heterozygote (+/−) or CerS2-null mice, both of which gave a similar labeling pattern (not shown). A good correlation was observed between astroglial and microglial activation and X-Gal staining (Fig. 5 and 6*A*). Thus, CerS2 is highly expressed in white matter regions such as the fimbria, the corpus callosum, and the internal capsule (Fig. 5), consistent with the role of very long acyl chain SLs in myelin (17), and correlates with high levels of gliosis and vacuolization (Fig. 5). Likewise, elevated X-Gal staining was detected in the GP, which showed intense gliosis (Fig. 5). In contrast, there was less correlation in other areas (*i.e.* the thalamus, cortex, and CA1 region of the hippocampus) (Fig. 5), suggesting that very long acyl chain SLs may play less crucial roles in these areas or that there are additional mechanisms to regulate their levels.

Myelin Fiber Integrity—Altered myelin structure was further examined in the midbrain. Myelin degeneration and detachment from axons (Fig. 7*A*) was observed in 5-month-old CerS2-null mice, similar to that observed in peripheral nerves (19). To determine the time course of myelin degradation, MBP and PLP levels were analyzed at different ages. A significant reduction in myelin protein levels was observed from ~3 months (not shown) for MBP and from 5 months of age for PLP that became more pronounced with age (Fig. 7, *B* and *C*).

Differences in the character of myelinated fibers were further characterized by MRI in which an increase in T_2 and a reduction in the contrast between white and gray matter were observed (Fig. 8, *A* and *B*). The major white matter regions, such as the corpus callosum and the internal capsule, were almost unrecognizable in CerS2-null mice. Quantitative color-coded T_2 mapping (Fig. 8, *B* and *C*) showed a significant increase in the T_2 of the entire brain, which is consistent with inflammation and loss of macromolecules (*i.e.* degeneration of myelin).

Abnormal Motor Dysfunction—Based on the prevalence of histological abnormalities in areas associated with motor control (46), the motor response of CerS2-null mice was examined. Upon cage opening or handling of mice over 3 months of age, mice often showed symmetrical, fast myoclonic jerks and loss of posture lasting 40–60 s (supplemental Movie 1). EEG recordings showed abnormally fast rhythmic activity, suggesting general cortical dysfunction (Fig. 9, *A* and *B*). Power spectrum analysis confirmed abnormally fast activity in the γ range (>40 Hz; Fig. 9*D*). Notably, during myoclonic activity or audiogenic stimulus response, no changes in cortical EEG were observed (supplemental Movie 1). As EEG analysis can only recognize seizures from regions of cortical origin, these data indicate an abnormal subcortical function in CerS2-null mice that leads to

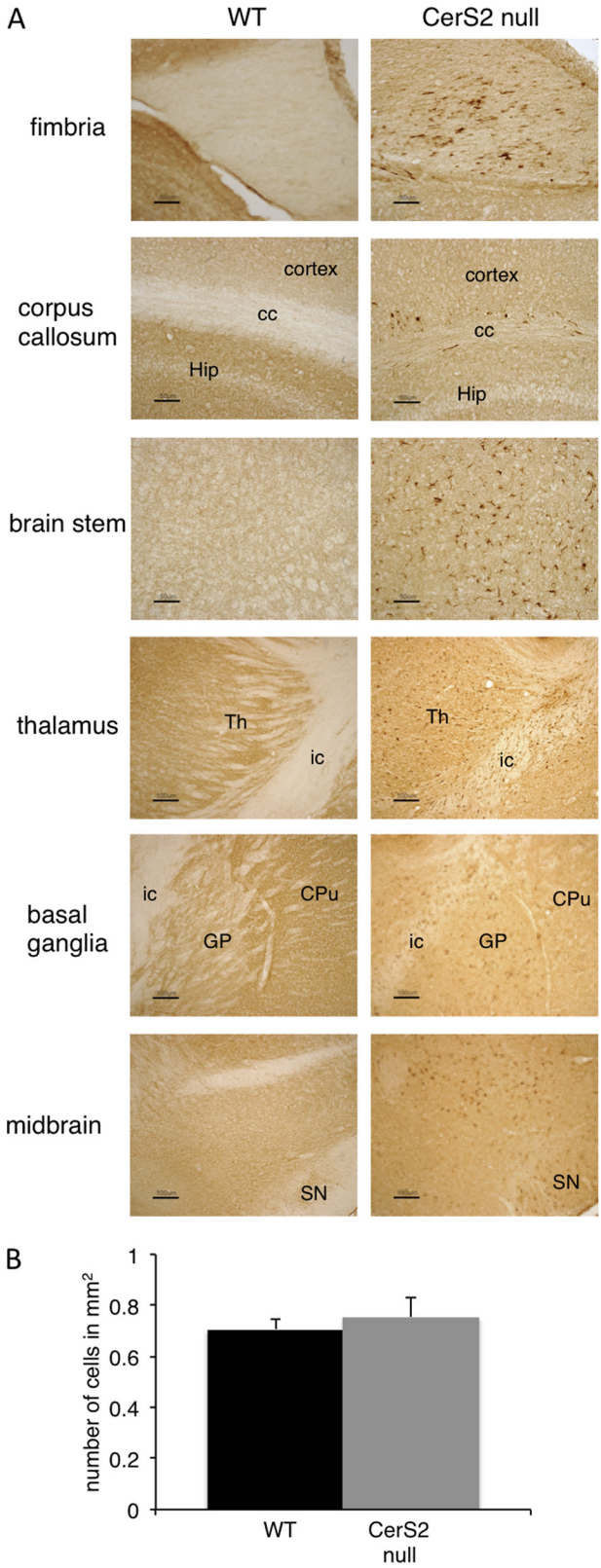

FIGURE 6. **Microglial activation in various brain regions.** *A*, immunostaining with an anti-Mac2 antibody in 4-month-old WT and CerS2-null brain (similar results were obtained at 7 months). Areas are coded as in Fig. 5. *Scale bars*, 50 μm for the fimbria, corpus callosum, and brain stem and 100 μm for the thalamus, basal ganglia, and midbrain. *B*, number of neurons in the GP of WT and CerS2-null mice.

motor dysfunction and correlates with the massive astrogliosis and microglial activation observed in the basal ganglia and brain stem.

Accumulation of Unidentified Intracellular Storage Material—Finally, we detected an unidentified intracellular membranous substance in lysosomes that appear to be in astrocytes (Fig. 10*A*). Lysosomes were packed with narrow, curved, "banana-shaped" storage material (Fig. 10*B*), and occasionally in older mice, lysosomes themselves became banana-shaped, containing densely packed lamella membranes (Fig. 10, *C* and *D*). The storage material was detected as early as 1.5 months of age. This kind of storage material is not observed in WT mice. To determine whether this storage material was the result of the defective activity of a lysosomal enzyme, the activity of several lysosomal hydrolases was examined in 2- and 6-month-old mice. No differences in the activity of acid sphingomyelinase, α-galactosidase, α-mannosidase, β-mannosidase, β-glucuronidase, arylsulfatase A, and galactosylceramidase were observed at either 2 or 6 months of age (not shown); a small increase in hexosaminidase A activity was observed at 6 months. Together with the lack of change in ganglioside levels (supplemental Fig. 1), this strongly suggests that the accumulating material is not a ganglioside, although the storage pattern visually resembles that observed in the GM1 gangliosidosis mouse (47).

DISCUSSION

The main finding of the current study is that ablation of CerS2 leads to neurological dysfunction and to development of bilateral and symmetrical encephalopathy characterized by vacuolization, astrogliosis, and microglial activation. The lesions are not restricted to white matter regions as might be expected based on the high levels of long acyl chain SLs in myelin (17) but are also found in gray matter regions.

In contrast to the hepatopathy (14), changes in long chain sphingoid base levels are unlikely to contribute to the encephalopathy in the CerS2-null mouse. Rather, the encephalopathy is almost certainly related to changes in SL levels and in SL acyl chain composition and more specifically to the virtually complete loss of non-OH-GalCer and the reduction in OH-Gal(Hex)Cer levels. This is the first time that we have observed a reduction in the total amount of a particular SL in the CerS2-null mouse. In liver, loss of C22–C24-SLs resulted in elevation of C16-SLs such that total SL levels were unaltered (14).

C18-non-OH-GalCer levels are not elevated upon depletion of C22–C24-non-OH-GalCer in the CerS2-null mouse. This may suggest that CGT, the enzyme that synthesizes GalCer, is either unable to utilize C18-non-OH-Cer or that C18-non-OH-Cer is inaccessible to CGT. Levels of C18-OH-Gal(Hex)Cer are elevated to some extent but not enough to compensate for the loss of C22–C24-OH-Gal(Hex)Cer. Together, these results imply some unexpected mechanisms of GalCer and OH-GalCer regulation in which the ratio between OH- and non-OH-GalCer plays a key role in myelin stability. In a mouse overexpressing CGT, non-OH-GalCer levels are elevated and OH-GalCer is decreased, and as a result, total GalCer levels (OH and non-OH) are unchanged (41, 44). CGT-overexpressing mice are characterized by unstable and uncompact myelin, supporting the idea that maintaining correct GalCer levels is

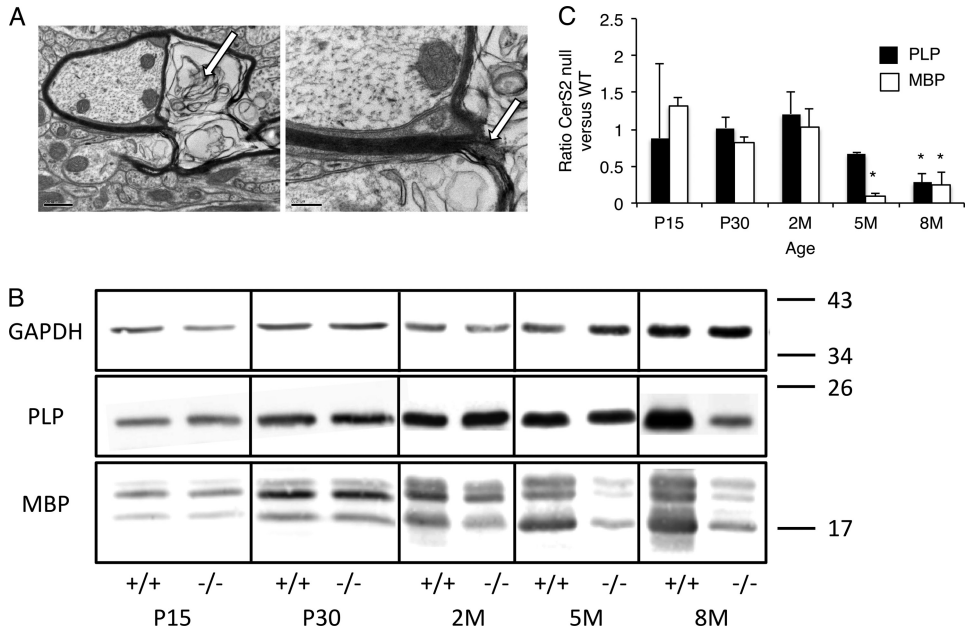

FIGURE 7. **Myelin degeneration.** *A*, electron micrograph from the midbrain of a 7-month-old CerS2-null mouse. Detachment (*left-hand panel*) and breakdown (*right-hand panel*) of the myelin sheath are observed. *Scale bars*, 0.5 μm for the *left-hand panel* and 0.2 μm for the *right-hand panel*. *B*, Western blots of MBP and PLP. Brain extracts from WT and CerS2-null mice brains at different ages: postnatal day 15 (*P15*), postnatal day 30 (*P30*), 2 months (*2M*), 5 months (*5M*), and 8 months (*8M*). Glyceraldehyde-3-phosphate dehydrogenase (*GAPDH*) acts as a loading control. *C*, -fold change in levels of MBP and PLP in CerS2-null *versus* WT mice (obtained by densitometry); values are normalized to GAPDH levels. Values are means ± S.D. ($n = 2$–3). *, $p < 0.05$.

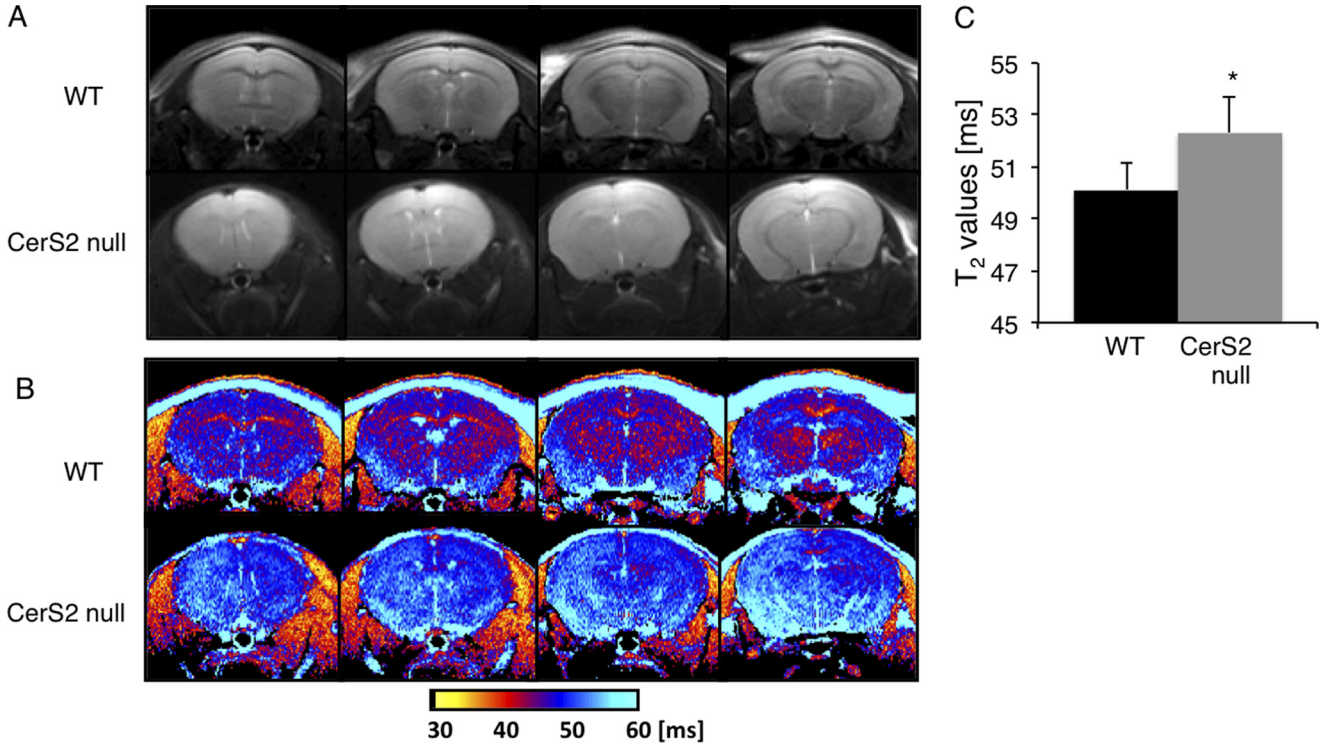

FIGURE 8. **MRI of WT and CerS2-null mice.** T_2-weighted magnetic resonance images (*A*) and quantitative color-coded T_2 magnetic resonance mapping (*B*) of four brain slices of the same mouse are shown. *C*, analysis of the T_2 maps. Values are means ± S.D. ($n = 5$). *, $p < 0.05$.

crucial for myelin formation and maintenance. A mouse defective in the enzyme responsible for hydroxy-SL synthesis, fatty acid 2-hydroxylase (FA2H), has also been generated, and elevated non-OH-GalCer levels were also observed. Old (18-month) FA2H−/− mice show defects in myelin maintenance, although myelin is normal in younger mice (up to 5 months) (48). In contrast, in CGT−/− mice, OH-GlcCer and OH-SM levels are elevated to compensate for the reduction in GalCer levels. However, OH-GlcCer levels cannot compensate for GalCer in myelin maintenance as a double knock-out of CGT and FA2H, lacking GalCer as well as OH-GlcCer and OH-SM, did not differ in its phenotypic appearance from the CGT−/− mouse (49). In the CerS2-null mouse, there is no compensation for the reduction in GalCer levels, and therefore myelin main-

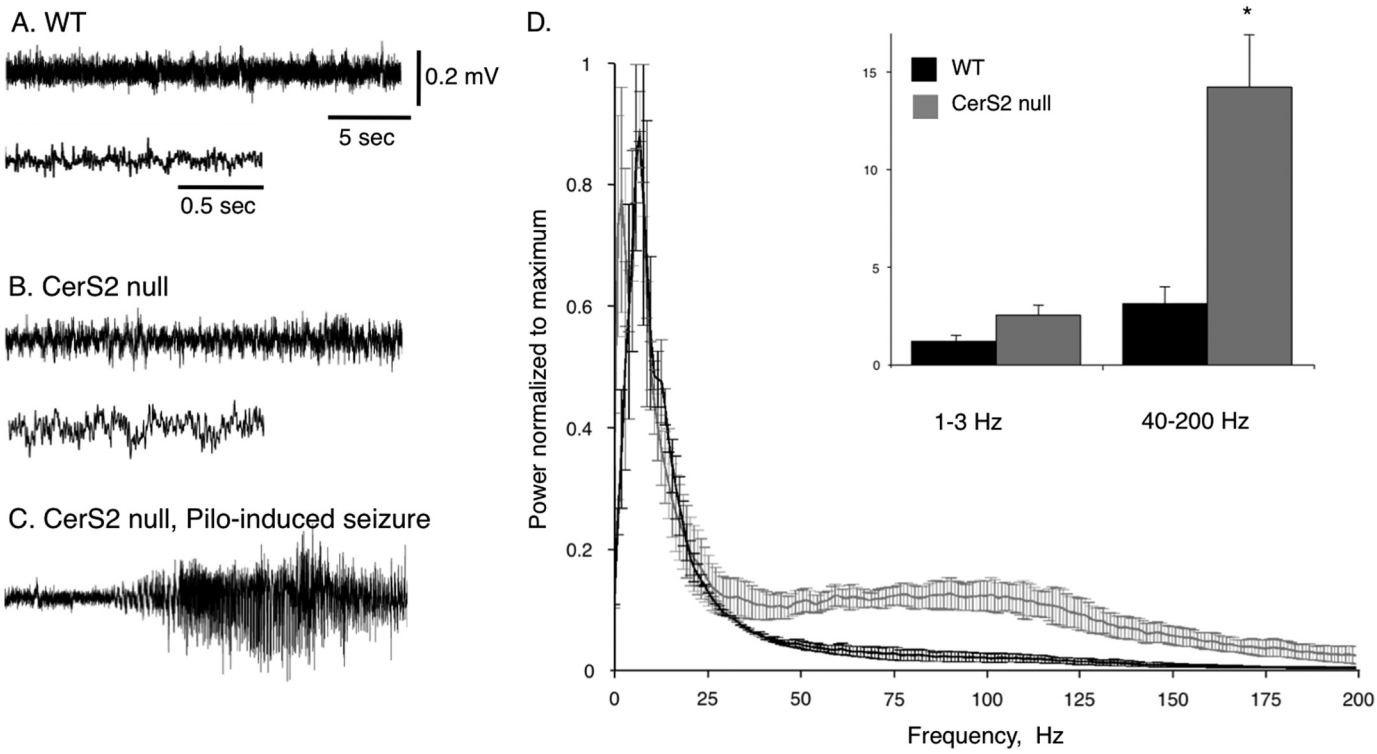

FIGURE 9. **EEG analysis of motor dysfunction.** EEG traces were recorded using epidural electrodes in WT (*A*) and CerS2-null (*B*) mice. Recording in the CerS2-null mice was performed during myoclonic jerk movements. The *lower trace* in *B* shows the same recording but with a faster time scale. *C*, a typical epileptic seizure was recorded 2 min after injection of the muscarinic agonist pilocarpine (*Pilo*) (310 mg/kg), confirming that the implanted electrodes are able to record cortical seizures (36). *D*, power spectrum density. The integral of activity for each mouse was calculated ($n = 5$) for slow δ (1–3 Hz) and fast γ (40–200) frequency ranges. Note the significant increase in fast γ activity in the cortex of CerS2-null mice. *, $p < 0.01$.

tenance is impaired, and myelin degenerates. The slight increase in C18-OH-Gal(Hex)Cer levels may be able to compensate to some extent for the loss of non-OH-C22–C24-GalCer, which is required for maintaining interactions between myelin membranes (50). This might account for the more moderate phenotype of the CerS2-null mouse compared with the CGT−/− mouse.

The molecular mechanisms leading from changes in GalCer levels and acyl chain composition to myelin degeneration are unknown (43). A defect in the myelin sheath of CerS2-null mice was reported previously (19) together with a reduction in myelin proteins and detachment of the inner lamella in peripheral neurons. We have considerably expanded this earlier work by examining the time course of the development of myelin defects in the central nervous system and show that myelin defects begin in CerS2-null mice at around 3 month of age, a time in which there is a major switch in the acyl chain composition of GalCer in WT mice. Thus, myelin formation seems to be unaffected, whereas myelin maintenance is considerably impaired. Lamellar separation and myelin detachment were also observed in CGT−/− mice (41, 45, 51), which die at a much younger age. The myelin phenotype in the CerS2-null mouse can be explained by changes in GalCer levels and in GalCer acyl chain distribution, whereas the altered acyl chain composition of ceramide, SM, GlcCer, or of down-stream glycosphingolipids such as gangliosides, which are found at high levels in neurons (52), may contribute to the neuronal phenotype observed. Moreover, CerS2 is expressed in both neurons and glia, suggesting that unlike the CGT−/− mouse in which the phenotype can be fully rescued by expression of the CGT gene uniquely in oligodendrocytes (53), rescuing the CerS2-null mouse will require expression of CerS2 in neurons, glia, and oligodendrocytes.

The gradual loss of myelin presumably results in the massive astrogliosis and microglial activation. Astrogliosis is sometimes seen in white matter deficiencies and has been observed in cerebroside sulfotransferase-null and in galactosylceramidase-null (twitcher) mice (54, 55). However, the brain disease in the CerS2-null mouse does not affect solely white matter regions. It is an adult onset, mild to moderate encephalopathy characterized by bilateral and symmetrical astrogliosis, microglial activation, and vacuolization affecting gray and white matter areas in the cerebrum, basal ganglia, brain stem, and cerebellum. Gliosis was visible in every white matter region examined, which might be a consequence of the myelin disruption. However, gliosis was also observed in brain regions associated with motor control with the most profound gliosis observed in the GP. The GP is an area in the basal ganglia that when disrupted causes movement disorders (56). Defects in the GP have been observed in several conditions such as copper and iron storage (57) and in lysosomal storage disorders such as Gaucher and Niemann-Pick C diseases (35, 58).

Vacuoles were not restricted to the medullary tree of the cerebellum as reported previously (19). Morphologic features of some vacuoles showed that they were due to ballooning of the myelin sheath, but the cause of most remains unknown. Bilateral and symmetrical distribution is typical of many degenerative and metabolic encephalopathies (59). Because CerS2-null mice show severe hepatopathy, some of the brain lesions

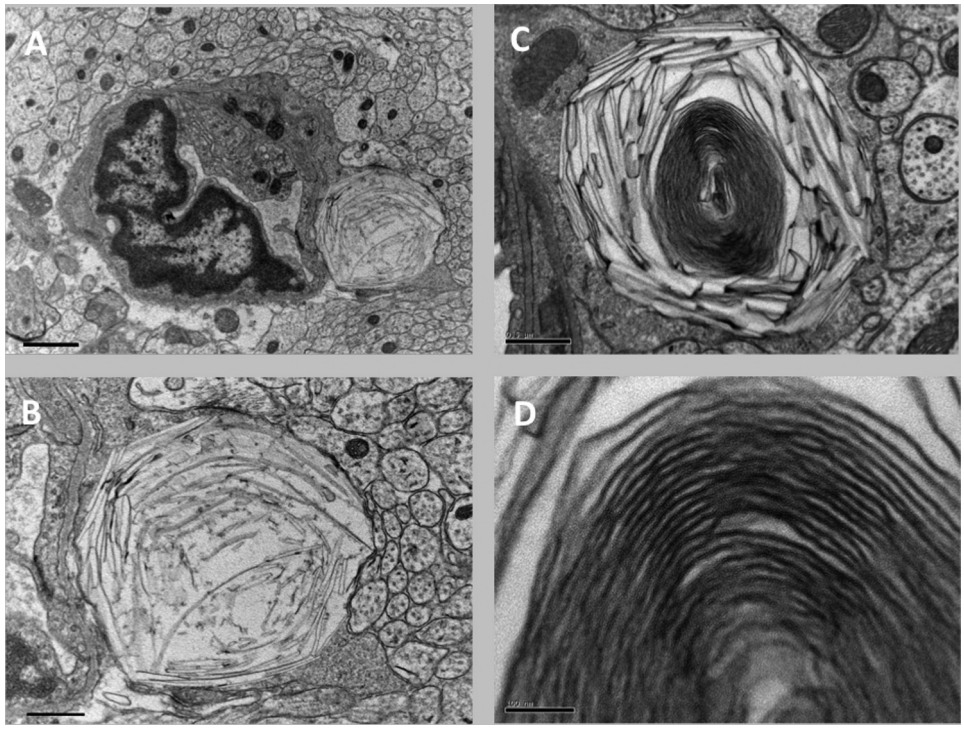

FIGURE 10. **Ultrastructural features of unidentified storage materials.** *A*, electron micrograph of the cerebrum of a 4-month-old CerS2-null mouse revealing a capillary lined by vascular endothelium and surrounded by unmyelinated axons. Attached to the endothelium is probably an astrocyte that contains a large lysosome packed with curved narrow banana-shaped storage material. *Scale bar*, 1 μm. *B*, higher magnification of the astrocyte that contains the curvilinear structures; the rest of the field is filled with unmyelinated axons. *Scale bar*, 0.5 μm. *C*, lower magnification of a lysosome in the midbrain of a 7-month-old CerS2-null mouse. Storage of banana-shaped material is seen at the *periphery*, and a lamellated membrane structure is in the *center*. *Scale bar*, 0.5 μm. *D*, higher magnification of the lamellated membrane structure seen in *C*. *Scale bar*, 0.1 μm.

could be caused by a hepatic encephalopathy (59). Hepatic encephalopathy has been observed, for instance, in fulminant hepatic failure, which is fatal within 1–2 days (60). However, despite the severe and progressive hepatopathy in the CerS2-null mouse, no clinical signs of liver failure were observed (15). Although some pathological features are shared between hepatic encephalopathy and the CerS2-null mouse, a number of other features are not, suggesting that the brain lesions are not a result of hepatic encephalopathy. For instance, gliosis is more widespread than vacuolization, and astroglial and microglial activation is accompanied by vacuolization in many but not all areas.

CerS2-null mice also show a distinctive neurological dysfunction of the motor system (but no neuronal loss). Generalized and symmetrical myoclonic jerks might be indicative of cortical dysfunction and seizures. However, although EEG recordings confirmed fast cortical activity at rest, cortical hypersynchronicity typical of seizure activity was not observed either spontaneously or during myoclonic jerks. This indicates that the motor dysfunction originates in subcortical structures, possibly in the basal ganglia or brain stem. This is supported by the massive astrogliosis and microglial activation in these regions. CerS2-null mice exhibit high sensitivity to audiogenic stimuli, resembling to some extent the lethal audiogenic seizures in mice overexpressing CGT in neurons (61).

Finally and quite unexpectedly, we detected the presence of unidentified storage materials in lysosomes of what are probably astrocytes. The storage material displayed a morphology similarity to the material that accumulates in Farber disease (62–64) and to the lamellated membrane structures that accumulate in the GM1 and GM2 gangliosidoses, Niemann-Pick disease and fucosidosis (65, 66). This substance is unlikely to be a ganglioside, and resolution of its composition will require isolation of lysosomes and biochemical analysis of their composition. However, it is of interest that a defect in a biosynthetic enzyme results in a phenotype that resembles a defect in a catabolic enzyme. Lysosomal storage is known to occur in some diseases in which the primary defect is not a lysosomal enzyme, one of which (*i.e.* neuronal ceroid lipofuscinosis) is caused by a defect in a protein, CLN8, which shares some homology to the ceramide synthase family (11).

In summary, we have systematically described the encephalopathy that occurs upon depletion of very long acyl chain SLs. Different features of the encephalopathy are probably related to the roles of specific SLs in specific nerve cell populations and in myelin, demonstrating previously unanticipated roles of SLs of defined acyl chain length in brain function and development.

Acknowledgments—The EM studies were conducted at the Moskowitz Center for Bio-Nano Imaging. We thank Racheli Erez-Roman for the sphingomyelinase assays.

REFERENCES

1. Schwarz, A., and Futerman, A. H. (1997) *J. Neurosci.* **17,** 2929–2938
2. Furuya, S., Ono, K., and Hirabayashi, Y. (1995) *J. Neurochem.* **65,** 1551–1561
3. Schwarz, A., Rapaport, E., Hirschberg, K., and Futerman, A. H. (1995) *J. Biol. Chem.* **270,** 10990–10998

4. Brann, A. B., Scott, R., Neuberger, Y., Abulafia, D., Boldin, S., Fainzilber, M., and Futerman, A. H. (1999) *J. Neurosci.* **19,** 8199–8206
5. Brann, A. B., Tcherpakov, M., Williams, I. M., Futerman, A. H., and Fainzilber, M. (2002) *J. Biol. Chem.* **277,** 9812–9818
6. Jana, A., and Pahan, K. (2010) *Neuromolecular Med.* **12,** 351–361
7. Venkataraman, K., Riebeling, C., Bodennec, J., Riezman, H., Allegood, J. C., Sullards, M. C., Merrill, A. H., Jr., and Futerman, A. H. (2002) *J. Biol. Chem.* **277,** 35642–35649
8. Riebeling, C., Allegood, J. C., Wang, E., Merrill, A. H., Jr., and Futerman, A. H. (2003) *J. Biol. Chem.* **278,** 43452–43459
9. Mizutani, Y., Kihara, A., and Igarashi, Y. (2005) *Biochem. J.* **390,** 263–271
10. Mizutani, Y., Kihara, A., and Igarashi, Y. (2006) *Biochem. J.* **398,** 531–538
11. Pewzner-Jung, Y., Ben-Dor, S., and Futerman, A. H. (2006) *J. Biol. Chem.* **281,** 25001–25005
12. Laviad, E. L., Albee, L., Pankova-Kholmyansky, I., Epstein, S., Park, H., Merrill, A. H., Jr., and Futerman, A. H. (2008) *J. Biol. Chem.* **283,** 5677–5684
13. Levy, M., and Futerman, A. H. (2010) *IUBMB Life* **62,** 347–356
14. Pewzner-Jung, Y., Park, H., Laviad, E. L., Silva, L. C., Lahiri, S., Stiban, J., Erez-Roman, R., Brügger, B., Sachsenheimer, T., Wieland, F., Prieto, M., Merrill, A. H., Jr., and Futerman, A. H. (2010) *J. Biol. Chem.* **285,** 10902–10910
15. Pewzner-Jung, Y., Brenner, O., Braun, S., Laviad, E. L., Ben-Dor, S., Feldmesser, E., Horn-Saban, S., Amann-Zalcenstein, D., Raanan, C., Berkutzki, T., Erez-Roman, R., Ben-David, O., Levy, M., Holzman, D., Park, H., Nyska, A., Merrill, A. H., Jr., and Futerman, A. H. (2010) *J. Biol. Chem.* **285,** 10911–10923
16. Becker, I., Wang-Eckhardt, L., Yaghootfam, A., Gieselmann, V., and Eckhardt, M. (2008) *Histochem. Cell Biol.* **129,** 233–241
17. Baumann, N., and Pham-Dinh, D. (2001) *Physiol. Rev.* **81,** 871–927
18. Ben-David, O., and Futerman, A. H. (2010) *Neuromolecular Med.* **12,** 341–350
19. Imgrund, S., Hartmann, D., Farwanah, H., Eckhardt, M., Sandhoff, R., Degen, J., Gieselmann, V., Sandhoff, K., and Willecke, K. (2009) *J. Biol. Chem.* **284,** 33549–33560
20. Hirschberg, K., Rodger, J., and Futerman, A. H. (1993) *Biochem. J.* **290,** 751–757
21. Shaner, R. L., Allegood, J. C., Park, H., Wang, E., Kelly, S., Haynes, C. A., Sullards, M. C., and Merrill, A. H., Jr. (2009) *J. Lipid Res.* **50,** 1692–1707
22. Brügger, B., Sandhoff, R., Wegehingel, S., Gorgas, K., Malsam, J., Helms, J. B., Lehmann, W. D., Nickel, W., and Wieland, F. T. (2000) *J. Cell Biol.* **151,** 507–518
23. Brügger, B., Glass, B., Haberkant, P., Leibrecht, I., Wieland, F. T., and Kräusslich, H. G. (2006) *Proc. Natl. Acad. Sci. U.S.A.* **103,** 2641–2646
24. Lahiri, S., Lee, H., Mesicek, J., Fuks, Z., Haimovitz-Friedman, A., Kolesnick, R. N., and Futerman, A. H. (2007) *FEBS Lett.* **581,** 5289–5294
25. Futerman, A. H., Stieger, B., Hubbard, A. L., and Pagano, R. E. (1990) *J. Biol. Chem.* **265,** 8650–8657
26. Ginzburg, L., and Futerman, A. H. (2005) *J. Neurochem.* **95,** 1619–1628
27. Hayashi, Y., Okino, N., Kakuta, Y., Shikanai, T., Tani, M., Narimatsu, H., and Ito, M. (2007) *J. Biol. Chem.* **282,** 30889–30900
28. Li, H. H., Yu, W. H., Rozengurt, N., Zhao, H. Z., Lyons, K. M., Anagnostaras, S., Fanselow, M. S., Suzuki, K., Vanier, M. T., and Neufeld, E. F. (1999) *Proc. Natl. Acad. Sci. U.S.A.* **96,** 14505–14510
29. Prence, E. M., and Natowicz, M. R. (1992) *Clin. Chem.* **38,** 501–503
30. Petushkova, N. A., Ivleva, T. S., and Vozniy, Ya. M. (1992) *Prenat. Diagn.* **12,** 835–839
31. Schnaar, R. L. (1994) *Methods Enzymol.* **230,** 348–370
32. Folch, J., Lees, M., and Sloane Stanley, G. H. (1957) *J. Biol. Chem.* **226,** 497–509
33. Svennerholm, L. (1957) *Biochim. Biophys. Acta* **24,** 604–611
34. Norton, W. T., and Poduslo, S. E. (1973) *J. Neurochem.* **21,** 749–757
35. Farfel-Becker, T., Vitner, E. B., Pressey, S. N., Eilam, R., Cooper, J. D., and Futerman, A. H. (2011) *Hum. Mol. Genet.* **20,** 1375–1386
36. Pitsch, J., Schoch, S., Gueler, N., Flor, P. J., van der Putten, H., and Becker, A. J. (2007) *Neurobiol. Dis.* **26,** 623–633
37. Welch, P. D. (1967) *IEEE Trans. Audio Electroacoustics* **15,** 70–73
38. Novgorodov, S. A., Chudakova, D. A., Wheeler, B. W., Bielawski, J., Kindy, M. S., Obeid, L. M., and Gudz, T. I. (2011) *J. Biol. Chem.* **286,** 4644–4658
39. Sastry, P. S. (1985) *Prog. Lipid Res.* **24,** 69–176
40. Muse, E. D., Jurevics, H., Toews, A. D., Matsushima, G. K., and Morell, P. (2001) *J. Neurochem.* **76,** 77–86
41. Coetzee, T., Fujita, N., Dupree, J., Shi, R., Blight, A., Suzuki, K., Suzuki, K., and Popko, B. (1996) *Cell* **86,** 209–219
42. van der Bijl, P., Strous, G. J., Lopes-Cardozo, M., Thomas-Oates, J., and van Meer, G. (1996) *Biochem. J.* **317,** 589–597
43. Hama, H. (2010) *Biochim. Biophys. Acta* **1801,** 405–414
44. Zöller, I., Büssow, H., Gieselmann, V., and Eckhardt, M. (2005) *Glia* **52,** 190–198
45. Dupree, J. L., Suzuki, K., and Popko, B. (1998) *Microsc. Res. Tech.* **41,** 431–440
46. David, Y., Cacheaux, L. P., Ivens, S., Lapilover, E., Heinemann, U., Kaufer, D., and Friedman, A. (2009) *J. Neurosci.* **29,** 10588–10599
47. Müller, G., Alldinger, S., Moritz, A., Zurbriggen, A., Kirchhof, N., Sewell, A., and Baumgärtner, W. (2001) *Vet. Pathol.* **38,** 281–290
48. Zöller, I., Meixner, M., Hartmann, D., Büssow, H., Meyer, R., Gieselmann, V., and Eckhardt, M. (2008) *J. Neurosci.* **28,** 9741–9754
49. Meixner, M., Jungnickel, J., Grothe, C., Gieselmann, V., and Eckhardt, M. (2011) *BMC Neurosci.* **12,** 22
50. Stewart, R. J., and Boggs, J. M. (1993) *Biochemistry* **32,** 10666–10674
51. Dupree, J. L., and Popko, B. (1999) *J. Neurocytol.* **28,** 271–279
52. Ledeen, R. W., and Wu, G. (1992) *Trends Glycosci. Glycotechnol.* **4,** 174–187
53. Fewou, S. N., Büssow, H., Schaeren-Wiemers, N., Vanier, M. T., Macklin, W. B., Gieselmann, V., and Eckhardt, M. (2005) *J. Neurochem.* **94,** 469–481
54. Taniike, M., Marcus, J. R., Nishigaki, T., Fujita, N., Popko, B., Suzuki, K., and Suzuki, K. (1998) *J. Neurosci. Res.* **51,** 536–540
55. Marcus, J., Honigbaum, S., Shroff, S., Honke, K., Rosenbluth, J., and Dupree, J. L. (2006) *Glia* **53,** 372–381
56. Walker, F. O. (2007) *Semin. Neurol.* **27,** 143–150
57. Gregory, A., Polster, B. J., and Hayflick, S. J. (2009) *J. Med. Genet.* **46,** 73–80
58. Baudry, M., Yao, Y., Simmons, D., Liu, J., and Bi, X. (2003) *Exp. Neurol.* **184,** 887–903
59. Summers, B. A., Cummings, J. F., and DeLahunta, A. (1995) *Veterinary Neuropathology*, pp. 208–351, Mosby, St. Louis, MO
60. Matkowskyj, K. A., Marrero, J. A., Carroll, R. E., Danilkovich, A. V., Green, R. M., and Benya, R. V. (1999) *Am. J. Physiol. Gastrointest. Liver Physiol.* **277,** G455–G462
61. van Zyl, R., Gieselmann, V., and Eckhardt, M. (2010) *J. Neurochem.* **112,** 282–295
62. Burck, U., Moser, H. W., Goebel, H. H., Grüttner, R., and Held, K. R. (1985) *Eur. J. Pediatr.* **143,** 203–208
63. Rauch, H. J., and Auböck, L. (1983) *Am. J. Dermatopathol.* **5,** 263–266
64. Fujiwaki, T., Hamanaka, S., Tate, S., Inagaki, F., Suzuki, M., Suzuki, A., and Mori, C. (1995) *Clin. Chim. Acta* **234,** 23–36
65. Beirowski, B., Nógrádi, A., Babetto, E., Garcia-Alias, G., and Coleman, M. P. (2010) *J. Neuropathol. Exp. Neurol.* **69,** 455–472
66. Coleman, M. (2005) *Nat. Rev. Neurosci.* **6,** 889–898
67. Svennerholm, L. (1963) *J. Neurochem.* **10,** 455–463